

Supplemental Material for

Active spintronic-metasurface terahertz emitters with tunable chirality

Changqin Liu^{1,2†}, Shunjia Wang^{1†}, Sheng Zhang^{1†}, Qinnan Cai^{1†}, Peng Wang¹, Chuanshan Tian¹, Lei Zhou^{1*}, Yizheng Wu^{1,2*}, Zhensheng Tao^{1*}

¹ *Department of Physics and State Key Laboratory of Surface Physics, Fudan University, Shanghai 200433, China*

² *Shanghai Research Center for Quantum Sciences, Shanghai 201315, China*

[†]These authors contributed equally to this work.

*Corresponding authors: Dr. Lei Zhou, phzhou@fudan.edu.cn; Dr. Yizheng Wu, wuyizheng@fudan.edu.cn; Dr. Zhensheng Tao, ZhenshengTao@fudan.edu.cn.

S1. Experimental setup

The experimental setup is illustrated in Fig. S1. The ultrashort pulses are generated by high-efficiency pulse compression of a Yb:KGW laser amplifier with periodic layered Kerr media (PLKM). In the experiments, we employed a Yb:KGW laser amplifier with a pulse duration of 170 fs at $\lambda=1030$ nm. Transform-limited femtosecond pulses with p polarization are focused to a beam waist of ~ 140 μm , with the incident pulse energy of 80 μJ and the repetition rate of 100 kHz. The PLKM is composed of 12 fused silica (SiO_2) thin plates as the Kerr medium, placed at the Brewster angle to minimize the reflection loss. The nominal thickness of the plates is fixed to be 0.8 mm and the distance between the neighboring layers is adjusted to 2.54 cm which can achieve solitary beam propagation, supporting high-quality supercontinuum generation of the laser pulse⁴³. The supercontinuum spectrum of the output pulse is plotted in Fig. S2a. The spectrally broadened beam is then compressed by a set of chirped mirrors (PC1611, Ultrafast Innovations) which supplies an appropriate amount of negative group-delay dispersion (GDD) to compensate the phase. The temporal profiles of the compressed pulses are shown in Fig. S2b, which are measured by second-harmonic-generation frequency-resolved optical gating (SHG-FROG). After the pulse compression, ultrashort pulses with a duration of ~ 24 fs and an energy of 60 μJ are generated.

As shown in Fig. S1, about 90% of the compressed femtosecond pulses is delivered for exciting the metasurface terahertz emitters. The energy is further attenuated by a combination

of NIR half waveplate and polarizer to $\sim 20 \mu\text{J}$ to avoid the sample damage. A small portion ($\sim 10\%$) of the energy is used as the ultrashort probe pulse for the electro-optic sampling (EOS). In the EOS system, a $300 \mu\text{m}$ -thick GaP crystal is selected as the EOS crystal which can support sufficiently broad bandwidth in the measurements. The emitted THz wave is collected and focused onto the GaP crystal by pairs of 90° parabolic mirrors and flat mirrors (Fig. S1). The probe pulse is sent through a precisely controlled delay stage, and then is combined with the terahertz wave after the last parabolic mirror into the GaP crystal. A standard detection system, which consists of a quarter-wave plate ($\lambda/4$), a Wollaston prism and two balanced photodiodes, are constructed to detect the time-domain profiles of the terahertz electric field. All the EOS measurements are performed in a dry-air environment with humidity less than 1%. To resolve the terahertz waveforms with different polarizations, a wire-grid polarizer with the extinction ratio of 10000:1 is installed before the EOS crystal. The GaP sample can also be rotated in plane for measuring the terahertz waveforms with different polarization accordingly.

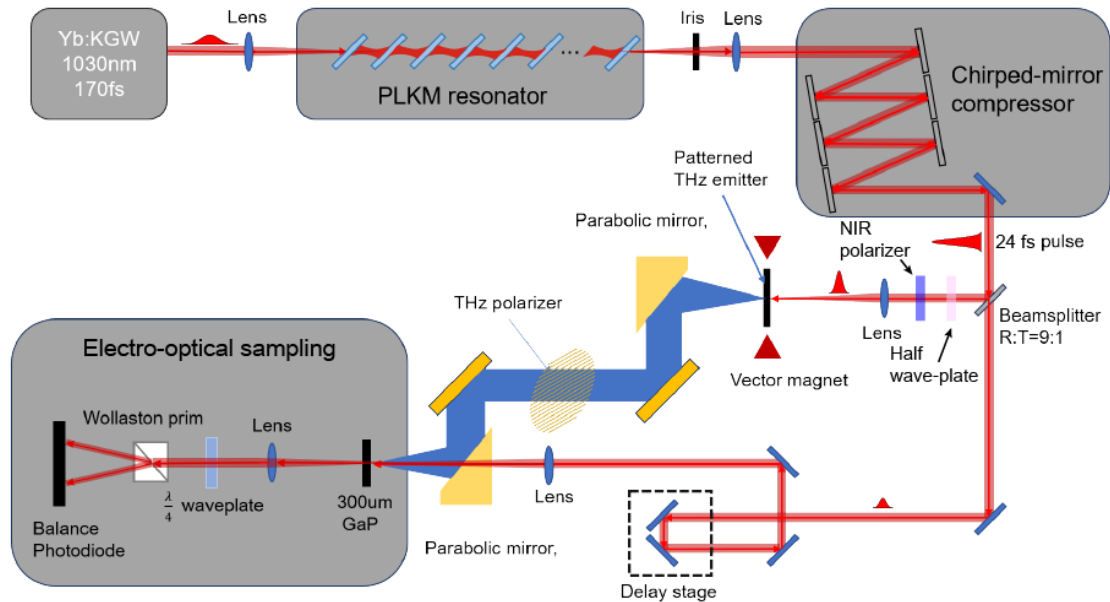


Figure S1. Experimental setup.

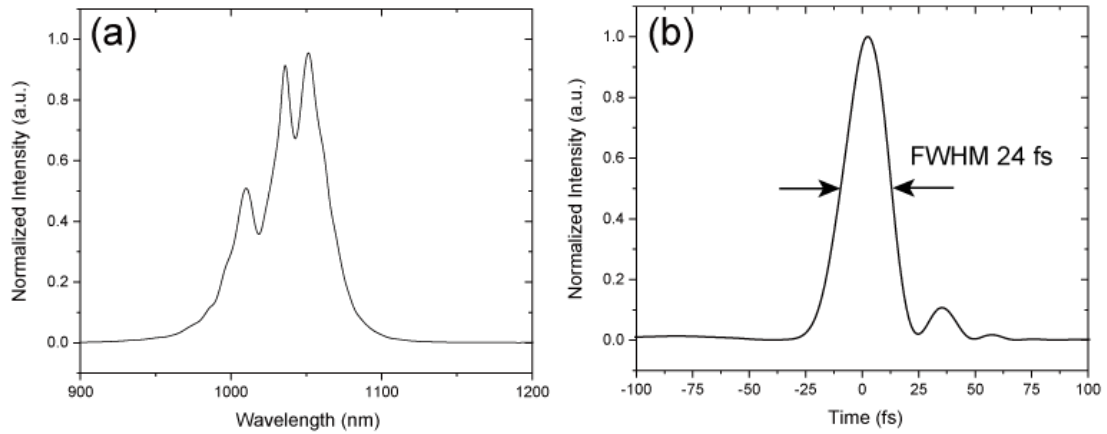


Figure S2. (a) Supercontinuum spectrum of the laser pulses after the PLKM compressor. (b) The temporal profiles of the compressed pulses.

S2. Sample fabrication

The $\text{Co}_{50}\text{Fe}_{50}/\text{Pt}$ heterostructures are grown on SiO_2 wafers with 2-inch diameter by confocal dc magnetron sputtering. The substrates are cleaned by a short plasma etching and the following annealing at 200 °C for 10 minutes. A $\text{Co}_{50}\text{Fe}_{50}$ alloy target is used for growing the CoFe film. After the growth of the CoFe film, the sample is capped by a 5 nm SiO_2 layer using rf sputtering. All the layers are grown at room temperature with the Ar pressure of 3 mTorr. The deposition rate is 0.55 Å/s for Pt layer and 0.30 Å/s for CoFe alloy layer. The thickness is 3 nm for the Pt layer and 1.4 nm for the CoFe layer, which are optimized for the maximum terahertz radiation. After the film growth, the sample is cut into small square pieces with the size of ~10 mm, and each piece of the $\text{SiO}_2/\text{CoFe}/\text{Pt}$ sample is patterned into the microstrips with different period and filling factor using the standard optical lithography and ion beam etching process.

S3. Magnetic and static-transport properties of the samples

The magnetic properties of the metasurface-patterned samples are characterized using both a static magneto-optic Kerr effect (MOKE) setup and the time-resolved terahertz spectroscopy, and are compared with those of the homogeneous thin-film sample with the same FM/NM

heterostructure. As shown in Fig. S3, the stripe-pattern samples exhibit a nearly rectangular hysteresis loop with a coercive field of ~ 6 mT, which is consistent with that measured on homogeneous samples. We note that the coercive fields for the stripe-patterned samples with the magnetic field \mathbf{H} perpendicular ($\theta_H=90^\circ$) and parallel ($\theta_H=0$) to the stripes are also consistent with each other, indicating that the magnetic shape anisotropy is negligible in our case. The same hysteresis loops and coercive field are also directly confirmed by our time-resolve terahertz spectroscopy measurement by tracking the peak-to-peak amplitude as a function of the external magnetic field. As a result, the external magnetic field of 200 mT in our experiments is large enough to saturate the magnetic moment in both directions.

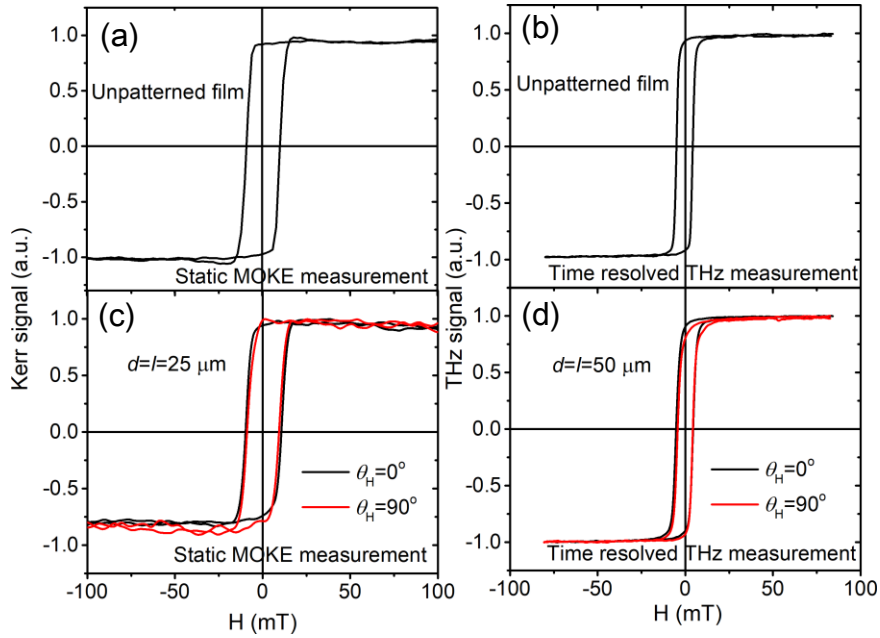


Figure S3. (a) The hysteresis loop of the homogeneous thin film sample measured using a static MOKE setup. (b) The hysteresis loop of the same sample as measured using the time-resolved terahertz spectroscopy setup. (c) The hysteresis loops of the stripe-patterned samples with $d=l=25 \mu\text{m}$, measured using the static MOKE setup. The loops for the magnetic fields along ($\theta_H=0$) and perpendicular to ($\theta_H=90^\circ$) the stripes are both measured. (d) Same as (c) measured with the time-resolved terahertz spectroscopy setup.

For measuring the conductivity of the heterostructure thin films, the patterned Hall bars are fabricated in the homogeneous $\text{Co}_{50}\text{Fe}_{50}/\text{Pt}$ heterostructures by means of photolithography and lift-off techniques. The width and the distance between the two electrodes of the Hall bars are $100 \mu\text{m}$ and $300 \mu\text{m}$, respectively. The electrodes are covered by 10 nm Cr and 30 nm Au by

using sputtering method. A longitudinal dc current of 0.1 mA is applied for the measurement of the static conductivity, which yields $\sigma_{\text{Fe-Co}} = 2.0 \times 10^6$ S/m. This static conductivity is generally consistent with the previous work⁵⁶.

S4. Calibration of the polarization-resolved EOS setup

The elliptically polarized terahertz waves can be decomposed into mutually orthogonal components E^{\parallel} and E^{\perp} . By measuring the terahertz electric fields polarized in two directions, we are able to recover the full three-dimensional profiles of the chiral terahertz waves and characterize their ellipticity. In our experiments, the terahertz waveforms are measured with EOS, and the fields polarized along the directions perpendicular and parallel to the stripes are resolved by implementing a terahertz wire-grid polarizer and adjusting the EOS crystal angle accordingly. For the detection of the terahertz amplitudes, we use a 300- μm -thick GaP(110) crystal as the detection crystal in the EOS setup. It is essential to develop an EOS setup which can yield equal sensitivity on the terahertz-wave components on mutually orthogonal polarizations. This is achieved by setting the terahertz polarizer in the parallel and perpendicular directions, as well as by rotating the GaP crystal in-plane to the appropriate angle. The response function of the EOS system as a function of the orientation of the GaP crystal and the probe polarization is illustrated in Fig. S4(a), which can be calculated by⁴⁴

$$\Delta I(\alpha, \beta) = I_p \frac{\omega n^3 E_{\text{THz}} r_{41} L}{2v_c} (\cos \alpha \sin 2\beta + 2 \sin \alpha \cos 2\beta), \quad (\text{S1})$$

where I_p is the probe intensity, ω the angular frequency of the probe, n the refractive index, r_{41} the nonzero coefficient of the electro-optic tensor, L the crystal length, α the angle of the terahertz-wave polarization with respect to the [001] crystal axis and β the angle of the probe-beam polarization with respect to the [001] crystal axis, as illustrated in Fig. S4(a). According to Eq. (S1), when the probe beam has a fixed polarization, the terahertz fields of E^{\parallel} and E^{\perp} can be measured with the same sensitivity by rotating the GaP crystal with 90 degrees in plane, as shown in Fig. S4(a) and (b).

To calibrate the response our EOS setup, we implemented a spintronic terahertz emitter with a homogeneous thin-film sample with the same FM/NM ($\text{Fe}_{50}\text{Co}_{50}/\text{Pt}$) heterostructure excited with the same laser conditions. The sample was installed in the same oriented magnetic

field and a field strength of ~ 200 mT was applied, which is sufficient to saturate the sample magnetization. By varying the field angle θ_H , the thin film emits linearly polarized terahertz waves with different directions of the field polarization and an identical temporal field profile. The polarization direction is always perpendicular to the external magnetic field \mathbf{H} . The typical EOS signal of a homogeneous thin-film emitter (E_{homo}) is plotted in Fig. S5(a). The corresponding terahertz spectrum is plotted in Fig. S5(b). The projected EOS signals to the two orthogonal directions of a linearly polarized terahertz wave from a thin-film emitter under different field angles are measured. In Fig. S4(d), we plot the peak-to-peak amplitude (V_{pp}) as a function of the field angle for E^{\parallel} and E^{\perp} . The field strengths in the two directions exhibit precise sine- and cosine-function behaviors with equal amplitudes. Moreover, in the time-domain, the terahertz waves also exhibit identical temporal profiles, as shown in Fig. S4(c). These results clearly demonstrate that our polarization-resolved EOS setup can precisely measure the time-dependent components of a chiral terahertz wave in the mutually orthogonal polarization directions (E^{\parallel} and E^{\perp}) with equal sensitivity.

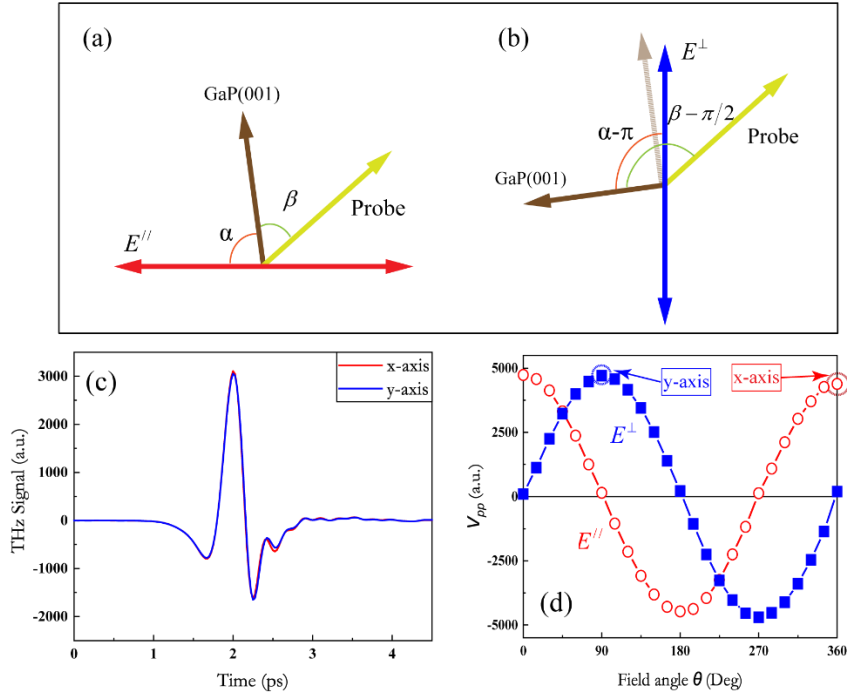


Figure S4. Calibration of the EOS system. (a) and (b) The schematic geometry of the probe and terahertz polarizations and the crystal orientation in the EOS system, for measuring E^{\parallel} and E^{\perp} respectively. (c) The temporal profiles when the polarization of the terahertz waves aligns with the two orthogonal polarizations both emitted from the same homogeneous thin-film emitter. (d) The peak-to-peak amplitudes of the EOS signal from a thin-film emitter under different field angles measured under

two orthogonal polarizations (E^{\parallel} and E^{\perp}).

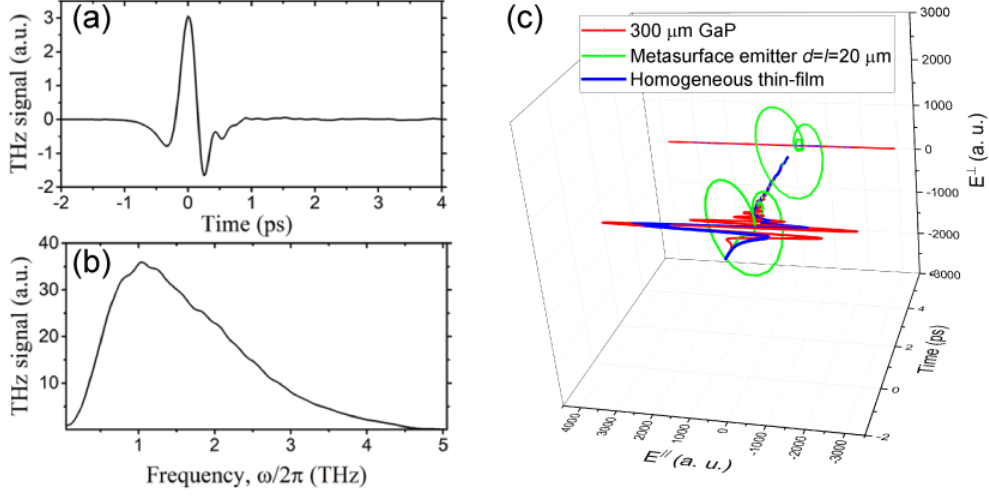


Figure S5. (a) The EOS signal from a homogeneous thin-film emitter. (b) The spectrum obtained by the Fourier transform of the signal in (a). (c) Comparison between the terahertz waveforms generated from a 300- μm -thick GaP (110), a homogeneous thin-film emitter and the metasurface emitter with $d=l=20 \mu\text{m}$, excited and detected under the same conditions.

We also calibrate the field strength and generation efficiency of our hybrid chiral terahertz emitters. The overall conversion efficiency of the metasurface emitter can reach $\sim 5 \times 10^{-6}$, which is directly measured with a pyroelectric terahertz power meter (Gentec THZ-5B-BL). For direct comparison with the commercially available terahertz emitters, a 300- μm -thick GaP (110) crystal is excited under the same laser conditions and the linearly polarized terahertz radiation is detected by the same EOS setup. In Fig. S5(c), we plot the temporal profiles of the chiral terahertz waves generated from a metasurface emitter, from a homogeneous thin-film emitter and from the GaP(110) crystal for a direct comparison. The conversion efficiency of our chiral terahertz emitter is comparable with the standard terahertz emitters for linear polarizations. We note that further optimization of the emission efficiency can be achieved by the FM/NM multilayer structures as demonstrated in the previous works³⁸.

S5. Results on the metasurfaces with FF=0.5 and different stripe widths

Fig. S6 (a), (e), (i), and (m) show the optical photograph with the stripe width $d=l=10, 20, 35$ and $50 \mu\text{m}$. Fig. S6 (b), (f), (j), and (n) show the corresponding terahertz-wave components polarized parallel (E^{\parallel}) and perpendicular (E^{\perp}) to the stripes, which exhibit different time-

domain waveform. Fig. S6 (c), (g), (k), and (o) present the frequency domain spectrum corresponding to the time-domain signals. Fig. S6 (d), (h), (l), and (p) depict the relative phase difference of $\varphi^\perp - \varphi^\parallel$ obtained by the experimental measurements, in comparison with the numerical simulations (red dashed lines). Noted that the phase differences in all the cases are the same ($\sim 0.5\pi$) at the low frequency ($\omega \rightarrow 0$), which is consistent with the geometric-confinement model. This phase drops away from 0.5π at high frequencies, and the drop rate increases as the stripe width d increases, indicating less confinement effects in wide stripes.

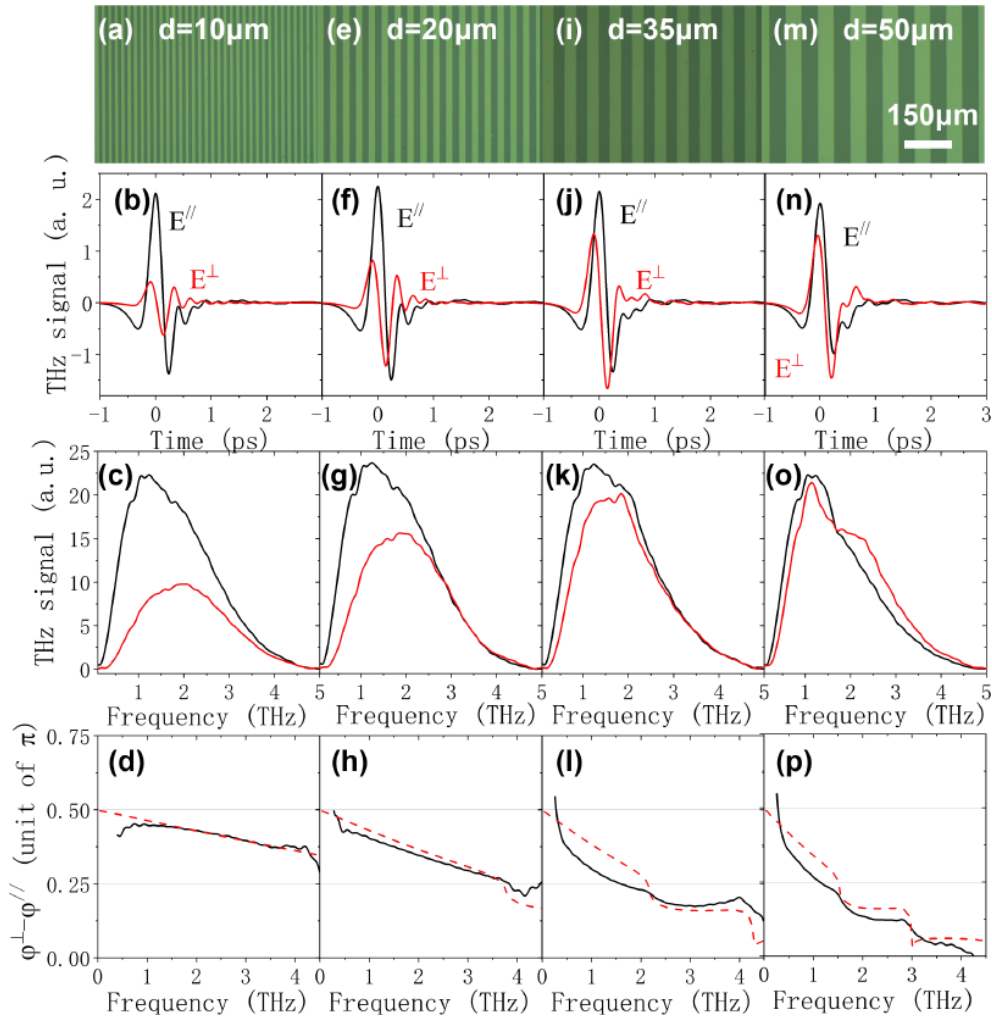


Figure S6. (a), (e), (i), and (m) Optical photograph of the grating structures. (b),(f),(j), and (n) Typical time-domain THz signals as the emitted THz-wave polarization along x-axis (E^\parallel , black line) and y-axis (E^\perp , red line). (c), (g), (k), and (o) The THz signals in the frequency domain corresponding to the time-domain signals. (d), (h), (l), and (p) The relative phase difference $\varphi^\perp - \varphi^\parallel$ obtained by the experimental time-domain spectrum (black solid line) and simulated results (red dashed line) for θ_H in between -90° and 0 . The metasurface structures of the stripe width $d= 10 \mu\text{m}$ (a-d), $20 \mu\text{m}$ (e-h), $35 \mu\text{m}$ (i-l), and $50 \mu\text{m}$ (m-p) with the filling factor of 50%, respectively.

As shown in Fig. S6 (i) and (p), step features of $\varphi^\perp - \varphi^\parallel$ as a function of the frequency can be observed, which is related to the anomaly features in the spectral domain. In Fig. S7, we further plot the normalized spectra of E^\parallel and E^\perp in accompany with the phase difference $\varphi^\perp - \varphi^\parallel$ for a number of different stripe widths d .

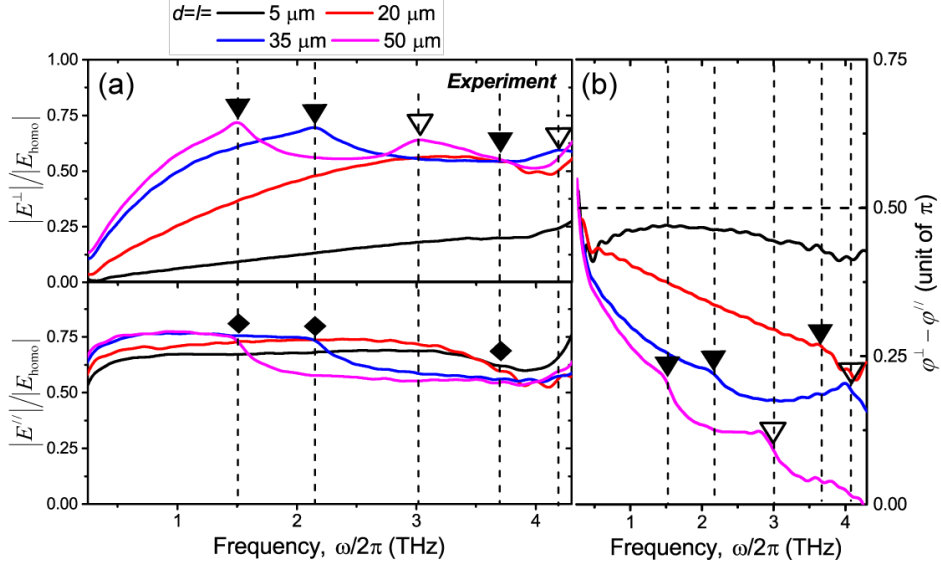


Figure S7. (a) The normalized spectra of E^\parallel and E^\perp for different stripe widths d for FF=0.5. The anomaly frequencies are labeled by the dashed lines and symbols. (b) The phase difference $\varphi^\perp - \varphi^\parallel$ for θ_H in between -90° and 0 corresponding to the results in (a). The same anomaly frequencies are labeled.

In Fig. S8(a) and (b), we plot the experimental measurements of the EOS signals for E^\parallel and E^\perp for $d=l=25 \mu\text{m}$. The results of the peak-to-peak amplitude V_{pp} as a function of θ_H are summarized in Fig. S7(c). The results of both E^\perp and E^\parallel exhibit a sinusoidal behavior, while a $\sim 90^\circ$ angle shift can be observed. The normalized spectra shown in Fig. S7(d) further displays identical spectral shapes for each polarization, although the spectra of E^\perp is blue-shifted compared to E^\parallel . These results are similar to those presented in Fig. 2 of the main text for $d=l=5 \mu\text{m}$, demonstrating the universality of our observations.

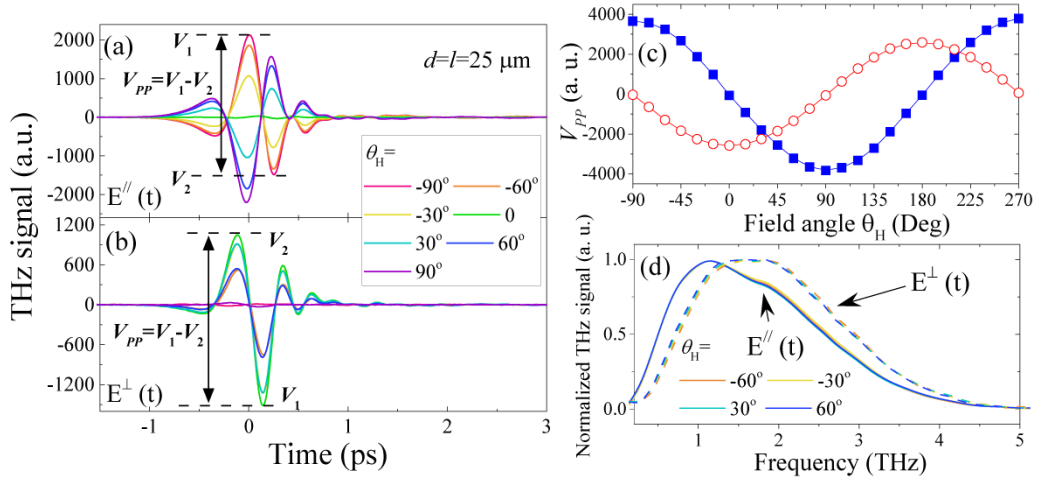


Figure S8. (a) Terahertz waveforms of E^{\parallel} under different field angles θ_H . The peak-to-peak field amplitude (V_{pp}) is defined as $V_1 - V_2$. (b) Same as (a) for E^{\perp} . (c) The peak-to-peak field amplitude (V_{pp}) as a function of θ_H . (d) Normalized spectra of E^{\parallel} and E^{\perp} under different field angles θ_H .

S6. Results on the metasurfaces with $d=50 \mu\text{m}$ and different filling factors (FF)

Fig. S9 (a), (d), and (g) show the optical photograph with fixed stripe width $d=50 \mu\text{m}$ and varying stripe spacing $l=20, 40$ and $70 \mu\text{m}$. Fig. S9 (b), (e), and (h) show the corresponding terahertz-wave components polarized parallel (E^{\parallel}) and perpendicular (E^{\perp}) to the stripes. Fig. S9 (c) and (f) exhibit the field spectrum of E^{\perp} and E^{\parallel} normalized by that obtained from a homogeneous film E_{hom} . In Fig. S9 (i), we summarize the anomaly features as a function of a characteristic frequency $\frac{v_c}{d+l}$. The same data are also included in Fig. 4(e) of the main text.

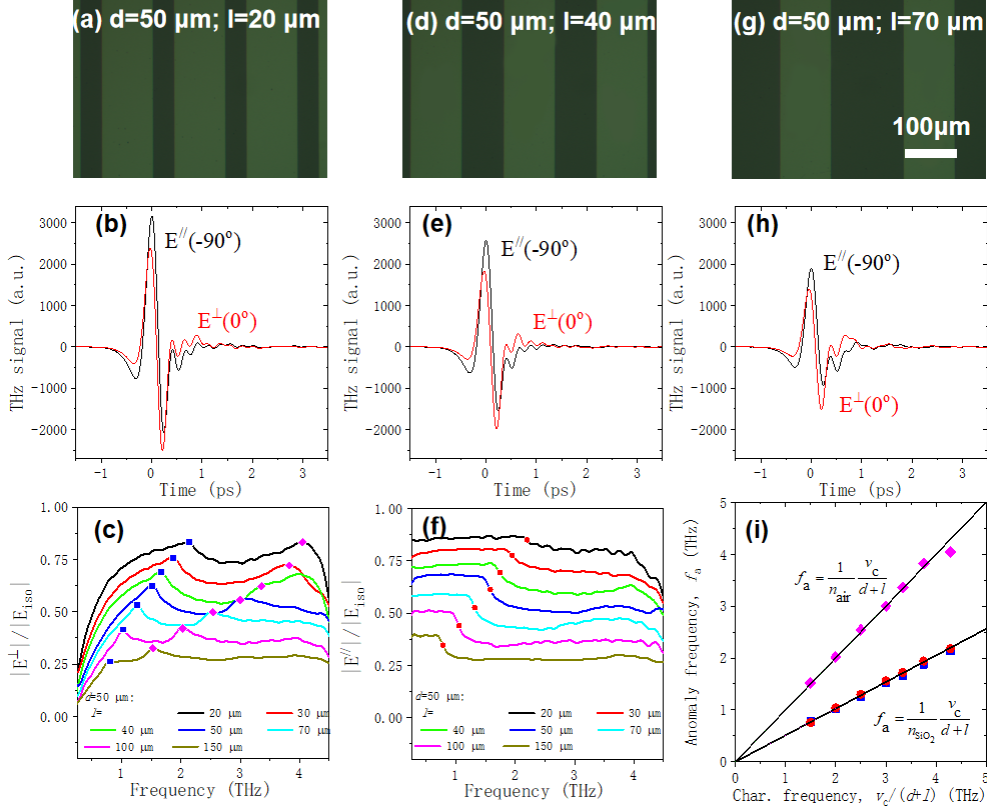


Figure S9. (a), (d) and (g) Optical photograph of the grating structures. (b), (e), and (h) Typical time-domain THz signals as the emitted THz-wave polarization along x -axis (E'' , black line) and y -axis (E^\perp , red line). (c) and (f) The field spectrum of E^\perp and E'' normalized by that obtained from a homogeneous film E_{homo} as a function of the frequency. (i) The anomaly features as a function of characteristic frequency obtained from the stripe width d and stripe spacing l . The metasurface structures of fixed stripe width $d=50 \mu\text{m}$ and varying stripe spacing $l=20$ (a), (b), 40 (d), (e), and $70 \mu\text{m}$ (g), (h).

S7. Results on the metasurfaces with an Al_2O_3 substrate

Fig. S10 (a) and (d) shows the emitted THz-wave signal on Al_2O_3 substrate with the stripe width $d=l=35$ and $65 \mu\text{m}$. Fig. S10 (b) and (e) show comparison of the terahertz frequency domain spectrum E'' and E^\perp for the stripe width $d=l=35$ and $65 \mu\text{m}$ on Al_2O_3 substrate. Fig. S10 (c) and (f) are the THz spectrum normalized by that obtained from an unpatterned film on Al_2O_3 substrate. The corresponding anomaly features are marked and summarized in Fig. 4(e), the

low-frequency ones of which can be well fitted by $f_a^1 = \frac{1}{n_{\text{Al}_2\text{O}_3}} \frac{v_c}{d+l}$.

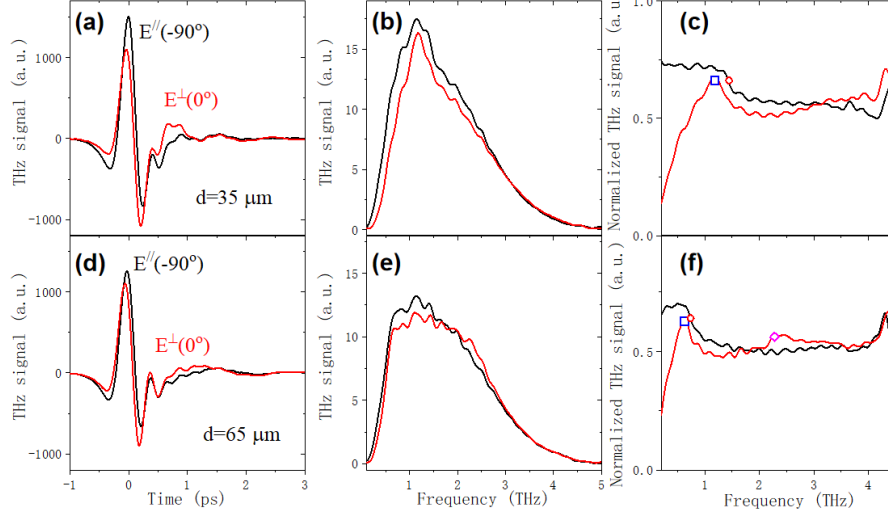


Figure S10. (a) and (d) EOS signals of the grating structures on Al_2O_3 substrate as the emitted THz-wave polarization along x -axis (E'' , black line) and y -axis (E^\perp , red line). (b) and (e) are the THz signals in the frequency domain corresponding to the time-domain signals. (c) and (f) are the THz spectrum normalized by that obtained from an unpatterned sample $\text{Fe}_{50}\text{Co}_{50}/\text{Pt}$ on Al_2O_3 substrate. The black and red line represent the signal as THz polarization parallel and perpendicular to the stripe. (a-c) and (d-f) are the grating structures with width $d=l=35$, and $65 \mu\text{m}$.

S8. Details of the model derivation

In this section, we provide the detailed derivation of our spatial-confinement model.

The spintronics-origin driving current \mathbf{j}_c flows always perpendicular to the external magnetic field \mathbf{H} as shown in Fig. 1c. According to Ohm's law, the electric-field component E'' (E^\perp) of the emitted terahertz wave is proportional to the total current density flowing in the same direction, j_a'' (j_a^\perp) by

$$\begin{aligned} E''(\omega) &= \kappa''(\omega) j_a''(\omega), \\ E^\perp(\omega) &= -\kappa^\perp(\omega) j_a^\perp(\omega) \end{aligned} \quad (\text{S2}).$$

Here we note that the minus sign for the perpendicular is because we define $+y$ direction as the positive-field direction, while the flowing direction of j_a^\perp and j_c along the $-y$ direction [see Fig. 1(c)]. For the currents flowing along the stripes, because there is no confinement effect, the current density j_a'' is solely contributed by the x -component of \mathbf{j}_c , and is given by

$$j_a'' = j_c \sin \theta_H \quad (\text{S3}).$$

For the current density flowing perpendicular to the stripes, the total current density j_a^\perp

consists of both the y-component of \mathbf{j}_c and the metasurface-induced “counteractive” current j_i [see Fig. 1(c)], which yields

$$j_a^\perp = j_c \cos \theta_H - j_i \quad (\text{S4}).$$

Here, j_i originates from the induced electric field (E_i) inside the metal films of the transient charge density Q_i , which is given by $j_i = \sigma E_i$, and E_i is related to Q_i by $E_i = \frac{Q_i}{C}$, where C is the proportionality constant. We note that because the metal heterostructure is very thin (a few nanometers), its conductivity is generally about one order of magnitude lower than the bulk metals (see Sec. S3), which makes the building up of the induced electric field E_i possible.

The constant C is determined by the geometry of the metasurface structure. In Fig. S11, we plot the schematic of the electric-field distribution with the same stripe width d , but different spacing l . When the stripes approach closer to each other, stronger coupling between the charges in different stripes can reduce the electric field E_i inside the metal thin films. This corresponds to an increase of C , which is responsible for the decrease of field ellipticity as the FF increases as shown in Fig. 5a. In other words, the constant C represents the strength of the capacitive coupling between different stripes. The values of C under the low-frequency limit can be numerically calculated by COMSOL, which confirms the above picture (Fig. 5a).

In our model, the metasurface-induced transient charge density Q_i can be considered as the result of the accumulation of the current density j_a^\perp on the stripe boundaries over time, which can be calculated by $Q_i(t) = \int_0^t j_a^\perp dt$. As a result, we have

$$j_i(t) = \frac{\sigma}{C} \int_0^t j_a^\perp dt \quad (\text{S5}).$$

Taking Fourier transform on the both sides of Eq. S5, we have

$$\tilde{j}_i(\omega) = -\frac{\sigma(\omega) \tilde{j}_a^\perp(\omega)}{i\omega C}, \quad (\text{S6}),$$

where $\tilde{j}_i(\omega)$ and $\tilde{j}_a^\perp(\omega)$ are the Fourier transform of $j_i(t)$ and $j_a^\perp(t)$, respectively. If we plug Eq. S6 into Eq. S4, we have the following relation in the frequency domain

$$\tilde{j}_a^\perp(\omega) = -\frac{i\omega C}{i\omega C - \sigma(\omega)} \tilde{j}_c(\omega) \cos \theta_H \quad (\text{S7}).$$

As a result, we have

$$E''(\omega) = \kappa''(\omega) j_c(\omega) \sin \theta_H \quad (\text{S8}),$$

and

$$E^\perp(\omega) = \frac{i\omega\kappa^\perp(\omega)C}{[i\omega C - \sigma(\omega)]} j_c \cos \theta_H \quad (\text{S9}).$$

Here, we ignore the “ \sim ” sign for the Fourier transform. Thus, under the low frequency limit ($\omega \rightarrow 0$) and $\sigma(\omega)$ and $\kappa(\omega)$ are both approximately constant, we have

$$E''(\omega) = \kappa'' j_c(\omega) \sin \theta_H \quad \text{and} \quad E^\perp(\omega) = -\frac{i\omega\kappa^\perp C}{\sigma} j_c(\omega) \cos \theta_H .$$

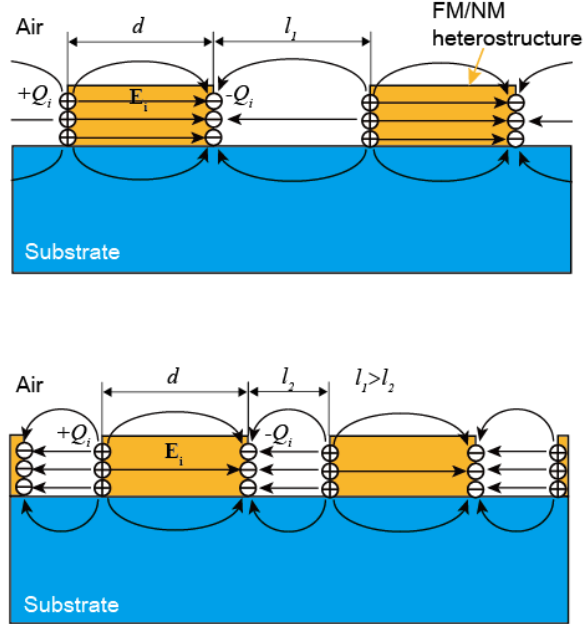


Figure S11. The schematic of the electric field distributions between the transient charges (Q_i) for the same stripe width d , but different stripe spacing l . When the stripes are moving closer to each other, the stronger capacitive coupling reduces the strength of induced electric fields inside the metal layer.

S9. Generation and manipulation of chiral terahertz waves

The chiral terahertz waveforms can be generated from the spintronic-metasurface emitters with various geometries when $d < 80 \mu\text{m}$. In Fig. S12, we plot the 3D field profiles of the terahertz waves with a number of different d and l . We note these chiral terahertz waveforms are measured under an optimum field angle (θ_H^{opt}), which is determined by the angle where the field amplitudes along the two orthogonal polarizations are approximately equal, given by

$\theta_H^{\text{opt}} = \tan^{-1} \left[\frac{\max(|E''(t)|)}{\max(|E^\perp(t)|)} \right]$ in practice. In Fig. S13, we plot the experimentally measured

θ_H^{opt} for different stripe widths d with FF = 0.5. Theoretically, the optimum angle can also be predicted by the numerical simulation (the dashed line in Fig. S13), which exhibits excellent agreement.

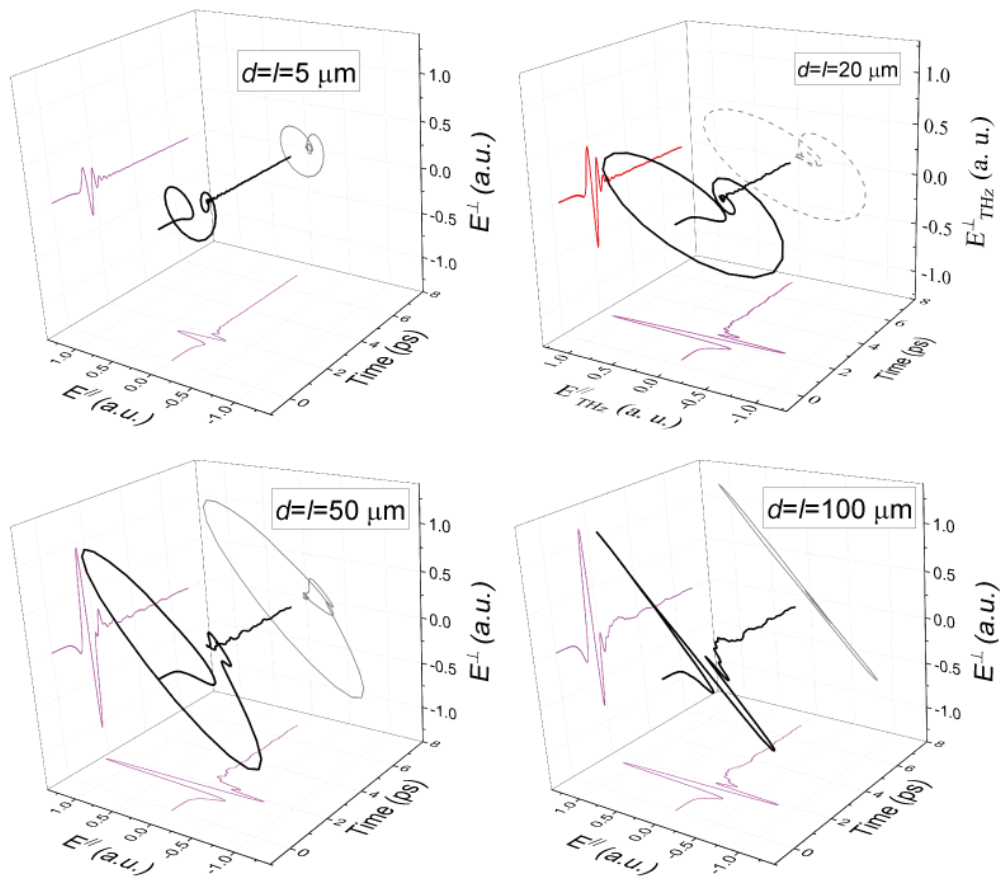


Figure S12. 3D chiral terahertz waveforms for different stripe widths and spacings.

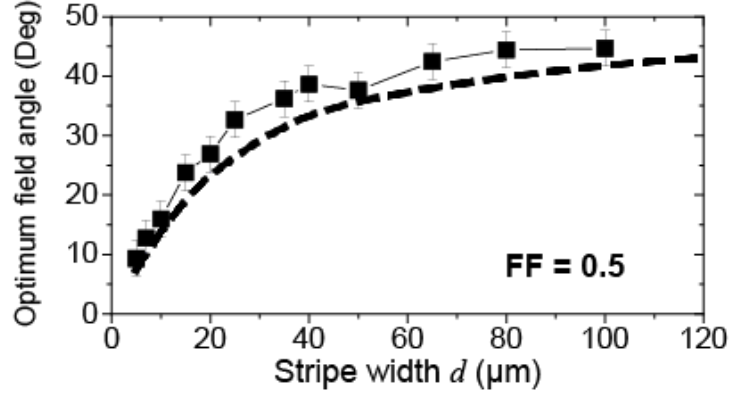


Figure S13. Optimum field angle θ_H^{opt} for chiral terahertz wave generation under different d with $\text{FF}=0.5$.

The tuning of the terahertz polarization and helicity in Fig. 3(b) of the main text can also be well reproduced by the numerical simulations. In Fig. S14, we plot simulation results of $d=l=10\ \mu\text{m}$ under different θ_H , corresponding to the experimental results in Fig. 3b.

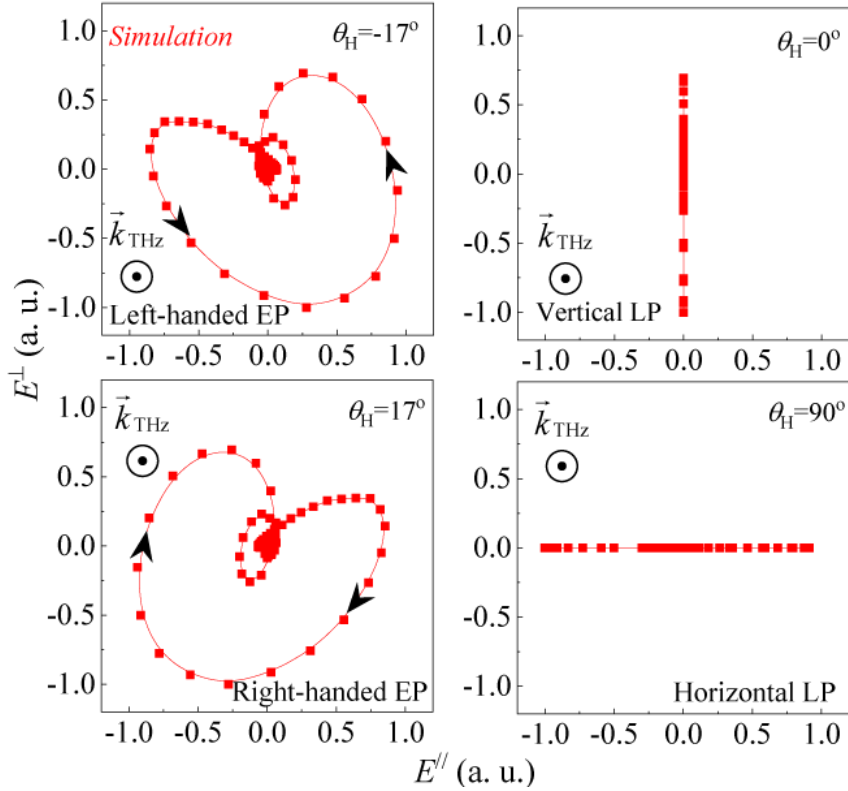


Figure S14. The simulation results of the parametric plots of E^{\parallel} and E^{\perp} with different θ_H under the same excitation conditions as Fig. 3(b). The direction of the terahertz wavevector \vec{k}_{THz} is labeled.

The broadband ellipticity $\langle \varepsilon \rangle$ is limited to ~ 0.75 generated under the optimum field angles from metasurfaces with $d=3-10 \mu\text{m}$. Because the relative phase can stay close to $\pm\pi/2$ through almost the entire spectrum for these narrow stripes [see Fig. 2(e)], the limit on $\langle \varepsilon \rangle$ must be imposed by the magnitude difference between the two orthogonal components. Indeed, as shown in Fig. 2(d), strong confinement in these narrow stripes lead to the spectrum of E^\perp is blueshifted relative to E^\parallel , and this leads to the limited broadband ellipticity of the narrow stripes. On the other hand, because the relative phase can stay close to $\pm\pi/2$, high ellipticity can be realized in a relatively narrower bandwidth in these narrow stripes where the magnitudes of the two components are close. As shown in Fig. 3(d), $\varepsilon > 0.85$ can be realized between 1.5 to 2.0 THz when $d=3-10 \mu\text{m}$. In Fig. S15, we plot the polarization states of the single frequencies for $d=5$ and $7 \mu\text{m}$ with $\text{FF}=0.5$, which clearly exhibits the high ellipticity in this spectral region.

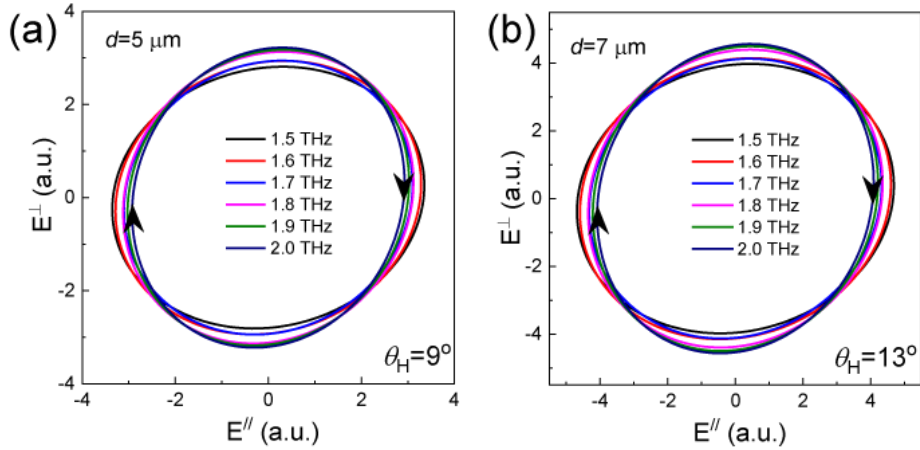


Figure S15. The polarization states of single frequencies in between 1.5-2.0 THz for the stripe widths $d=5 \mu\text{m}$ (a) and $d=7 \mu\text{m}$ (b).

S10. Numerical simulations

The numerical simulation in this work are conducted with the frequency-domain solver of COMSOL Multiphysics⁴⁹, a finite-element-method-based software. In our simulations, we use a non-dispersive conductivity for the modeling of a 5nm-thick Fe-Co layer, $\sigma_{\text{Fe-Co}} = 2 \times 10^6 \text{ S/m}$, which is determined experimentally (see Sec. S2). We impose the

periodic boundary condition along the x and y directions and a perfectly-matched-layer on the z direction for the outgoing-wave (non-reflective) boundary condition. The thickness of the substrate is set to be infinite, by which we ignore the subsequent terahertz signals caused by the multiple reflection of the electromagnetic waves at the upper and lower surfaces of the 200- μm -thick substrate. The terahertz refractive indices of the substrates are $n_{\text{SiO}_2} \approx 1.95$ and $n_{\text{Al}_2\text{O}_3} \approx 3.07$ ⁵², respectively. The spin-to-charge conversion is modeled by imposing a transverse external current density $\mathbf{j}_c(\omega)$ uniformly distributed in the FM/NM heterostructure layer and the direction of the driving current is perpendicular to the magnetic field \mathbf{H} . The amplitude and phase of $\mathbf{j}_c(\omega)$ can be obtained from the experimental results of the terahertz emission from the homogeneous thin films (see Sec. S2).

S11. Definition of the broadband terahertz ellipticity

The ellipticity of the emitted terahertz waves can be characterized by the Stokes parameters⁵⁰:

$$\begin{aligned}
s_0 &= |\mathbf{E}^{\prime\prime}|^2 + |\mathbf{E}^\perp|^2, \\
s_1 &= |\mathbf{E}^{\prime\prime}|^2 - |\mathbf{E}^\perp|^2, \\
s_2 &= 2|\mathbf{E}^{\prime\prime}||\mathbf{E}^\perp|\cos\delta, \\
s_3 &= 2|\mathbf{E}^{\prime\prime}||\mathbf{E}^\perp|\sin\delta,
\end{aligned} \tag{S10}$$

where $\delta = \varphi^\perp - \varphi^{\prime\prime}$ is the relative phase difference. The ellipticity is then given by

$$\varepsilon = \text{sgn}(s_3) \sqrt{\frac{s_0 - \sqrt{s_1^2 + s_2^2}}{s_0 + \sqrt{s_1^2 + s_2^2}}}, \tag{S11}$$

which leads to Eq. (2) in the main text. Here, $\varepsilon=1$ and -1 correspond to the full left- and right-handed circular polarizations, respectively, defined from the point of view of the receiver, while $\varepsilon=0$ corresponds to the linear polarizations. The broadband ellipticity is then calculated by the

arithmetic-mean average over the entire terahertz spectrum

$$\langle \varepsilon \rangle = \frac{\int_0^\infty \varepsilon(\omega) \left[|E''(\omega)|^2 + |E^\perp(\omega)|^2 \right] d\omega}{\int_0^\infty \left[|E''(\omega)|^2 + |E^\perp(\omega)|^2 \right] d\omega} .$$